AO04: Developing an experimental method for the retrieval of aerosol refractive indices at high wavenumber from coherent reflectance measurements, and testing the validity of the Coherent Scattering Model (CSM).

Candidate number: 272699
Supervisors: Dr. D. Peters and Dr. R. Grainger
Word count: 5930

Abstract

This report compares experimental data with the new and relatively untested Coherent Scattering Model (CSM). The model quantifies the contribution of aerosol particles in a suspension to the light reflectance at a glass-suspension interface. Experimental reflectance data was obtained for monodisperse suspensions of spherical 250 nm and 500 nm radius latex test particles. An internal reflection configuration using a semi-circular glass optic and with the suspension in contact with the top flat surface was used. The model provided a good fit to the experimental data for the 250 nm particles, and retrieved the real part of their refractive index correctly within experimental uncertainty. The model has not, to my knowledge, been tested on particles as large as this. The increased settling velocity of the 500 nm particles posed problems in obtaining reliable data, but this report details improvements made to the experimental procedure and gives recommendations for future work.

The first part of this report outlines the improvements made to apparatus performance. Apparatus performance was tested, independent of CSM theory, by making Fresnel reflectance measurements.

The second part of this report deals with CSM, and aims to test its suitability for retrieval of the refractive index of aerosols at high wavenumber - a value needed to reduce uncertainties in connected work.

1 Introduction

Aerosols have a significant effect on the climate. They have a direct effect on the radiative balance in the atmosphere by scattering incoming, short wave sunlight as well as by scattering and absorbing infrared radiation. There is considerable variation in these properties between different aerosol types: some aerosols have a net cooling effect on the atmosphere whilst others have a net heating effect. There are also indirect effects associated with aerosols, as they provide surfaces for chemical reactions and influence cloud formation.

The optical properties of aerosols are, in general, not well known and this has significant effects in a number of areas. Uncertainties in aerosol optical properties give rise to one of the largest uncertainties in climate forcing models and hence limit our best predictions of future climate change [1]. The 2007 IPCC report described the level of scientific understanding of the aerosol direct effect as 'medium-low', and gave a value of the net radiative forcing[1] across all aerosol types of $-0.5 \pm 0.4\,\mathrm{Wm}^{-2}$ (This is compared to the dominant term of $+2.63 \pm 0.26\,\mathrm{Wm}^{-2}$ for all long lived greenhouse gases, where the uncertainties are lowest) [1]. Aerosol uncertainties are also a significant limiting factor in the retrieval of atmospheric properties,

[1]Radiative forcing is defined as the perturbation in top of atmosphere, net downward irradiance that arises as a result of a particular external factor. In this case the direct effect of aerosols is considered. A negative value corresponds to the factor having a net cooling effect whilst a positive value correspnds to a net heating effect.

such as temperature and gas profiles, from remote sounding, satellite and ground-based measurements [2, 3].

Research in the Atmospheric, Oceanic and Planetary department uses measurements of the optical transmission through an aerosol sample to retrieve the refractive index of the aerosol. Such measurements, on aerosol types such as volcanic ash, add value to satellite measurements from instruments such as ATSR/2, AATSR and MIPAS [2].

The retrieval technique models the real and imaginary parts of the aerosol refractive indices as simple harmonic oscillators: a physically sensible approach given that particles consisting of more than one molecule, with electromagnetic radiation incident upon them, can be considered as a set of interacting, oscillating multipoles [3]. The retrieved refractive index has oscillatory behaviour at low wavenumber but tends to a constant value in the high wavenumber limit. It is the aim of this paper to develop an experimental method for measuring the refractive index of aerosols at high wavenumber. This will provide an independent check of the high wavenumber value retrieved from the transmission measurements.

This report is split into two parts. The first section sets out how the accuracy of the apparatus and new modifications made to it have been tested. To test the accuracy of the apparatus, Fresnel reflection measurements were made in order to retrieve the refractive indices of the glass optic and of water, both of which are known to high precision.

The second section deals with CSM, which quantifies the contribution from aerosol particles in a turbid suspension to the reflectivity at a glass-suspension boundary [4, 5]. The CSM has been recently developed and is relatively untested [4]. Experimental data for monodisperse suspensions containing 250 nm and 500 nm radius latex particles of a known refractive index were obtained. The model has not, to my knowledge, been tested on particles as large as this. CSM theory is compared with the experimental results. Its validity is examined, and its suitability for retrieval of atmospheric aerosol refractive indices is discussed.

2 Fresnel Theory

The propagation of light is described by the plane wave solutions to Maxwell's equations. The Fresnel equations express the reflectivity and transmission of light at the plane boundary between two half spaces containing different media. They are derived by first setting up the incident electromagnetic wave, applying the suitable boundary conditions, and then solving for the resultant transmitted and reflected waves [6]. This is done for both polarisations: where the incident electric field is perpendicular to the incident plane[2], and for the case where it is parallel. I summarise the key results below[3].

Snell's Law relates the refractive indices of the two media, the incident angle, θ_i, and the transmitted angle, θ_t[4]:

$$n_1 \sin(\theta_i) = n_2 \sin(\theta_t)$$

where n_1 and n_2 are the refractive indices of the initial and secondary medium respectively. The reflection is specular, i.e. $\theta_i = \theta_r$ where θ_r is the angle of reflection. The results for the complex amplitude reflection coefficients for the two polarisations are:

$$r_\perp = \frac{E_r}{E_i} = \frac{\cos(\theta_i) - m\cos(\theta_t)}{\cos(\theta_i) + m\cos(\theta_t)}$$

$$r_\parallel = \frac{E_r}{E_i} = \frac{m\cos(\theta_i) - \cos(\theta_t)}{m\cos(\theta_i) + \cos(\theta_t)}$$

where $m = \frac{n_2}{n_1}$, and E_i and E_r are the amplitudes of the incident and reflected waves respectively. These are related to the irradiance reflection coefficients, the ratio of reflected irradiance to the incident irradiance, via:

$$R_\perp = |r_\perp|^2$$

$$R_\parallel = |r_\parallel|^2$$

[2]The incident plane contains the incident, reflected and transmitted waves and is perpendicular to the plane boundary between the two media.

[3]For a clear and complete derivation see pg45, Topics in Remote Sounding, Bruce Hapke.

[4]θ_i, θ_t and θ_r are measured relative to the normal of the plane boundary between the two media.

3 Testing the Apparatus

3.1 Description of the Apparatus

The apparatus consists of a laser diode and a silicon photodiode detector, both mounted on arms such that they can be rotated by a full 360° around the sample (see Appendix A). The angular positions of the arms are controlled by stepper motors and a simple pulley system. The stepper motors are controlled by a microcontroller which is connected via USB to a laptop. Refer to Appendix A for detailed annotated photographs of the apparatus.

A modification was made to the apparatus: a laser power driver kit was added to control the laser power.

The detector has a polarizer mounted in front, and this was set so that only $\perp$ polarized light reached the detector. Thus all reflectivity data obtained in this paper are for $R_{\perp}$.

3.2 Laser Power Stability

The previous MPhys study found that the most significant source of error in reflectivity measurements using the apparatus was due to variations in laser output power. To improve the laser power stability the laser power source (a 9V battery) was connected to the laser diode via a laser driver kit. The driver kit uses a feedback loop that monitors the photodiode current (which is proportional to the laser output power) to regulate the laser output power. To test the laser power stability with this added feedback mechanism, the laser power was measured using the detector over a 16 hour period with a 0.2 s interval between detector readings. Figure 1 shows the detector count (proportional to irradiance incident on the detector) as a function of time. The detector count has a range corresponding to a maximum variation in the laser power of approximately 4 %. This variation in laser power is significant, but it can be seen from Figure 1 that it corresponds to a systematic drift on a timescale of hours. There is a smaller scale noise superimposed onto this drift.

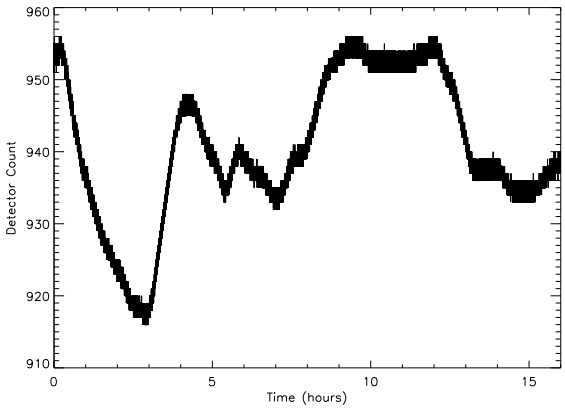

Figure 1: Laser power as a function of time.

As a result of this laser output variability there will be uncertainty in our estimate of the true incident laser irradiance, and thus in the value used to normalise the detector response to the reflected irradiance. The detector count is proportional to the irradiance incident on the detector, so reflectivity is calculated according to:

$$R = \frac{\text{Reflected Beam Detector Count} - \text{Background}}{\text{Incident Beam Detector Count} - \text{Background}}$$

One possibility is to measure the reflected beam for an incident angle such that there is total internal reflection, and then use this value as the normalising incident beam detector count (Method 1). This method assumes that the laser power remains constant for the duration of the scan over a range of incident angles. Another possibility is to take a second total internal reflection measurement at the end of the scan, and then linearly interpolate the laser power at each measurement's time location (Method 2).

To investigate the uncertainty in our estimate of reflectivity calculated using these two methods, the 16 hour laser power data were utilised. To do this, the scan duration and the time interval between scan measurements were needed. Firstly a start location was randomly selected from the data. Then the deficits were calculated between the data detector count value and the predicted value (according to the method adopted) at succeeding regular time intervals, corresponding to the times of scan measurements. This process was repeated 5,000 times for various total scan times, and for both methods.

The standard deviation in the deficits, σ_{LP}, gives the uncertainty in our estimate of laser power. Table 1 summarises the results.

Scan Time (mins)	σ_{LP}, detector counts Method 1	Method 2
10	1.13 (0.12%)	0.93 (0.10%)
20	2.09 (0.22%)	0.98 (0.11%)
40	3.77 (0.40%)	1.38 (0.15%)
60	5.38 (0.57%)	1.74 (0.19%)
90	6.74 (0.71%)	3.24 (0.34%)
120	7.21 (0.77%)	4.99 (0.53%)

Table 1: Shows uncertainty in our estimate of laser power, σ_{LP}, for the two estimation methods and for various scan times. Method 1: Assumes laser power constant over scan duration. Method 2: Linear interpolation. Note that bracketed values express σ_{LP} as percentage of mean laser power detector count.

Table 1 shows that σ_{LP} increases steadily with scan time, and that σ_{LP} is less using the interpolation method for all scan durations. The data obtained in this paper used a total scan time of 90 mins and Method 1 was adopted. The analysis of Method 2 is included here to demonstrate the possible gain of implementation in future work. However, as discussed further in Section 3.4.5, this is not the limiting factor on apparatus performance. A scan time of 90 mins was judged to be a suitable compromise between the increased laser power uncertainty of a longer scan and the resolution gained by increasing the number of measurements taken. This means that there is a laser power uncertainty of $\sigma_{LP} = 0.71\%$ in the data obtained.

3.3 Angular Arm Postions

The angular arm positions of the laser and detector are controlled by a stepper motor. Moving either arm 1256 steps will take it through a full 360° (so 1 step = 0.29° is the smallest angular resolution of the apparatus). The previous MPhys study assumed that the angular change in arm position is linear with the number of steps moved. To test this assumption a digital level, accurate to 0.1°, was used to measure the angular position of step locations at regular intervals of 10 steps. The angular level was zeroed on the base platform of the apparatus.

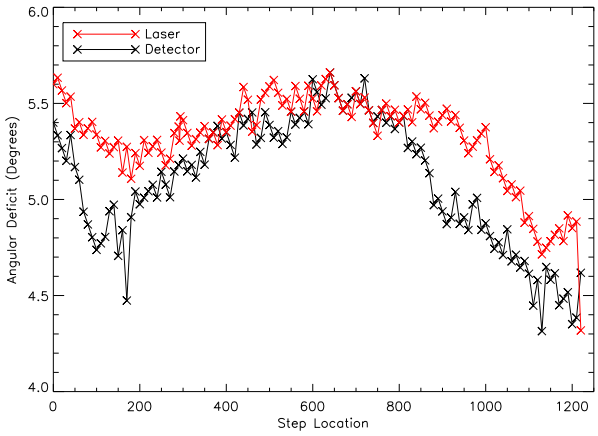

Figure 2: This graph illustrates the systematic variation in $\Delta\theta$ between step locations.

Figure 2 shows Angular Deficit, as defined below, plotted against Step Location.

$$\text{Angular Deficit} = \phi_{\text{measured}} - \phi_{\text{steps}}$$

where ϕ_{measured} is the angle measure by the digital level and ϕ_{steps} is the angle calculated using the step location and assuming a constant angle between step locations. For the constant angular interval hypothesis to be valid these plots should show a horizontal line[5], but it can be seen that this is not the case, indicating variation in the angle between step locations for both the laser and detector arms.

The angular locations of steps between those measured at the 10 step intervals, were calculated by linear interpolation. Thus a table is formed of all the angular positions of step locations for the laser and detector arms. This method corrects for the systematic drift seen in Figure 2. Further improvements in accuracy could be achieved in future work by measuring the angular position of all step locations using the digital level.

3.4 Measuring the Refractive Index of Glass and Water

To test the accuracy and overall performance of the equipment, independent of CSM theory, ex-

[5]Note that this horzontal line need not be at 0.0, due to the fact that ϕ_{measured} and ϕ_{steps} are zeroed relative to different reference points.

periments were carried out on glass-air and glass-water.

3.4.1 Monte Carlo Simulations

A Monte Carlo method was used to investigate the propagation of errors. For each error term, synthetic experimental data were generated by adding normally distributed random noise with a standard deviation equal to the relevant error term. The fitting procedure was then implemented, and the process was repeated 5,000 times in order to establish the propagated standard deviation in the fitted values. The glass-water results for each error term are summarised in Table 2.

It can be seen that the largest uncertainty, by an order of magnitude, in the fitted value of n_{water} arises from uncertainty in the angular arm locations.

3.4.2 Method: Glass-Air

The aim is to measure the laser beam reflectance from the glass-air boundary at the back surface of the semi-circular optic for a range of incident angles. Fresnel theory can then be used to retrieve the refractive index of the glass. The experimental set-up is shown in Figure 5 (except that the o-ring and glass slip used for containing liquid samples are removed).

Proper alignment of the optic is essential to prevent systematic errors entering the data. The incident laser beam must enter and leave the glass optic at normal incidence to the semi-circular surface, reflecting off the centre of the back surface. The vertical and horizontal position of the optic needed to be correctly set. An iterative approach was employed, using the requirement that $\theta_i = \theta_r$ for all θ_i as a check.

It is important to have an automated scan procedure to take data over a range of incidence angles. The microcontroller controls the arms' positions and the detector readings taken. Routines written in C are uploaded to the microcontroller via the USB port, and allow control of the scan.

One problem is that the laser beam has a Gaussian-like profile rather than a top-hat function. It was decided necessary that for any particular incidence angle, θ_i, the detector was to scan over a range of angles about $\theta_r = \theta_i$, thus capturing the profile and crucially the peak value. The range was chosen such that the entire reflected beam profile would be captured (i.e. until it reduces to the background level). This range was found to be ± 20 steps.

Furthermore, I decided to scan over a full range of incidence angles ($\theta_i = 0$ to $90°$), with a two step interval between laser arm positions (i.e. $\Delta\theta_i = 0.6°$). This step interval was chosen as a compromise between the gain of improved resolution and the associated increase in laser power uncertainty caused by the increased total scan time (see Sections 3.2 and 3.5).

So given the specifications established, Dr D. Peters, who was already familiar with the code, re-wrote the routine. In summary, for each laser step location separated by 2 step intervals, the detector scans ± 20 steps about $\theta_r = \theta_i$ and takes 10 readings at each step location.

It is important to have an accurate measure of the angular location of the normal to the flat back surface of the optic. This can be deduced, given that the back surface reflection is specular, from the angular positions of the laser and detector at the peak detector response location. We therefore have a set of independent measures of the normal for each incident laser location in the scan.

As the laser beam enters and leaves the optic at normal incidence to the semi-circular curved surface, the Fresnel transmittance at this surface must be considered. The requirement to directly quantify the Fresnel transmission and reflectance at this surface can be side-stepped however: as the beam is always at normal incidence to the curved surface the effect is the same for all data in the scan. Using a value of the detector count, for which the beam has undergone total internal reflectance at the back surface to normalise the data, will automatically correct for this.

Error Term	Error Term Value	Standard Deviation in fitted Re(n_{water})	Standard Deviation in fitted Im(n_{water})
Laser Power	$\sigma_{LP} = 0.71\%$	0.000132	4.29×10^{-5}
Angular Arm Position	$\sigma_{angle} = 0.1°$	0.00102	0.000429
Angular Offset	$\pm 0.1°$	± 0.0012	± 0.00053

Table 2: Glass-Water Monte Carlo Error Propogation Results. Uncertainty in angular arm positions gives rise to largest uncertainty in n_{water}.

3.4.3 Method: Glass-Water

The method is almost the same as for the glass-air case except that 2 or 3 drops of distilled water were placed inside a rubber o-ring placed on the top flat surface of the optic. The o-ring was covered with a glass slip to prevent evaporation of the water inside. The set-up is shown in Figure 5, where the sample in this case is distilled water.

The repeatability of the measurements was also investigated by repeating the glass-water scan 9 times successively.

3.4.4 Results and Analysis

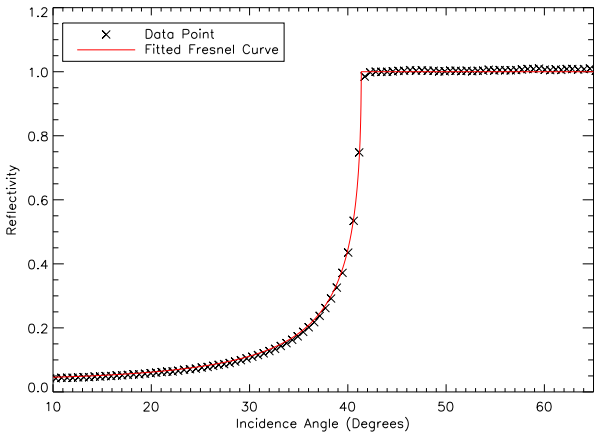

Figure 3: Glass-air scan, plot of $\perp$ irradiance reflectivity, $R_{\perp}$, against incidence angle, θ_i. The graph shows the experimental data and the fitted Fresnel curve in red. Fitted glass refractive index: $n_{\text{glass}} = 1.51332 + 9.2 \times 10^{-7} i$.

Figure 3 shows the data for the glass-air scan. Fresnel theory was used to fit the curve shown in red. A least squares fitting procedure was used, and both the real and imaginary parts of the glass refractive index were allowed to vary. The fitted value returned for the glass refractive index was $n_{\text{glass}} = 1.51332 + 9.2 \times 10^{-7} i$. The glass optic is made from BK7 glass, which has a known refractive index of $n_{\text{glass}}(\lambda = 635\text{nm}) = 1.51454 + 0.000i$ [17]. So there is a discrepancy of $\Delta Re(n_{\text{glass}}) = 0.00122$ in the real part, and the imaginary parts are in agreement to 3 decimal places. These results agree with the uncertainty expected from angular errors, as shown in Table 2.

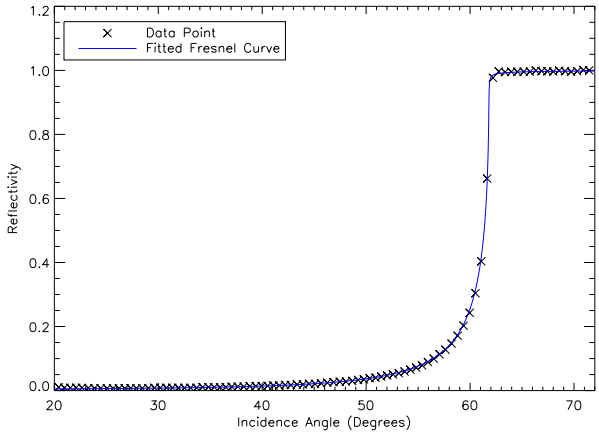

Figure 4: Glass-water Scan #2, plot of $\perp$ irradiance reflectivity, $R_{\perp}$, against incidence angle, θ_i. The graph shows the experimental data and the fitted Fresnel curve in blue. Table shows data for fitted refractive indices for all 9 scans.

Table 3 summarises the results for the repeated water scans. The mean fitted refractive index of water is $n_{\text{water}} = 1.33235 + 0.00032i$, which compares well with the known value of $n_{\text{water}} = 1.33205 + 0.00000i$ [18]. The discrepancy is $\Delta Re(n_{\text{water}}) = 0.00030$ and $\Delta Im(n_{\text{water}}) = 0.00032$. The discrepencies for all 9 scans are well within experimental uncertainties, Table 2.

It can also be seen from the standard deviation in the fitted values for the 9 scans that the repeatability of the measurements is very good. The standard deviation in reflectivity residuals at the data points gives a measure of the quality

Scan#	Fitted Fresnel Refractive Index Re(n_{water})	Im(n_{water})	σ Residual (percentage)
1	1.33198	0.00026	1.72
2	1.3321	0.00025	1.69
3	1.33239	0.00023	1.67
4	1.33243	0.00035	1.67
5	1.33242	0.00032	1.66
6	1.33246	0.00028	1.66
7	1.33251	0.00038	1.65
8	1.33242	0.00041	1.65
9	1.33237	0.00037	1.65
mean	1.33235	0.000316	1.67
σ	0.00017	0.000075	

Table 3: Shows results of 9 repeat scans for Glass-Water.

of the fit and is included in Table 3.

One weakness in the method used is that the arms were not re-zeroed between scans, and so any systematic variation arising from this has not been quantified.

3.5 Conclusion: Apparatus Accuracy

The Monte Carlo error propagation analysis demonstrates that uncertainty in the angular arm locations gives rise to the largest uncertainty in the fitted refractive index. This is the limiting factor and must be addressed first if further improvements in apparatus performance are to be achieved. One possibility for future work is to have a digital level with higher angular accuracy mounted to each arm, so that the angular locations of arms can be recorded at each detector reading. Implementation of the laser power interpolation method discussed in Section 3.2 could then achieve further improvements.

The results for the glass-air and glass-water scans demonstrate that the apparatus in its current state can be used to measure the real part of the refractive index of a homogeneous substance to an accuracy of within 0.1 %. A significant improvement in apparatus performance has been achieved: previous work with the apparatus had an accuracy poorer than 1 %.

4 CSM Theory

The aim is to deduce the refractive index of an aerosol from measurements of the power reflectivity about an interface between an incident medium and a turbid medium containing the aerosol particles (see Figure 5). In order to do this, we first must have a forward model that precisely quantifies the contribution to the reflectivity that arises from the aerosol particles. At first glance one might be tempted to assign an effective refractive index, n_{eff}, to the turbid medium, as the propagation of light in the turbid medium is consistent with that in a homogenous medium [7, 8, 9]. An important quantity in Mie scattering theory is the size parameter, $x = \frac{2\pi a_0}{\lambda}$, where a_0 is the particle radius and λ is the wavelength of incident light. Theoretical investigations have shown that for particles with $x \geq 1$ an incorrect reflectivity and transmittance is obtained from inserting n_{eff} into the usual Fresnel equations, as scattering is not included [5, 10, 11].

A complete treatment requires establishing a set of incident electromagnetic fields for an ensemble of randomly positioned particles, and then using the appropriate boundary conditions for the spheres to solve the coupled Mie Scattering equations [12, 13]. Unfortunately such calculations are computationally expensive and hence too time-consuming to be used for routine measurements.

CSM offers a suitable approximation for a dilute system of particles, but allows for particles with large size parameters [4, 5]. The reflectance that comes from the particles in a dilute system is generally small. The exception is for incident angles close to the critical angle, where the contribution from the particles is most significant.

Firstly, the model considers the reflectance that arises from a half space of randomly positioned particles. This is built up by considering consecutive slabs, such that their width is small compared to the incident wavelength. The model assumes that the positions of particles are uncorrelated, i.e. that the particles are sufficiently

dilute so that the exclusion volume[6] of particles can be ignored. The coherent reflectance and transmission for the slab are then computed in the single scattering approximation. Multiple scattering is taken into account by integration over multiple slabs.

The key result for the coherent reflection coefficient, r_{hs}, for a half space of randomly located, monodisperse particles is summarized below. The full derivation is lengthy and given in reference [5].

$$r_{hs} = \frac{\beta}{i(k_z^{\text{eff}} + k_z^m) + \alpha}$$

where α and β are related, as given below, to the diagonal elements $S_j(\theta_s)$ of the Mie scattering matrix of a spherical particle (as defined in reference [14]). Putting $j = 1$ or $j = 2$ gives the result for the perpendicular or parallel component respectively [14].

$$\alpha = \frac{-2\pi\rho S(0)}{k_m^2 \cos(\theta_m)}, \; \beta = \frac{-2\pi\rho S_j(\pi - 2\theta_m)}{k_m^2 \cos(\theta_m)}$$

and

$$k_z^m = k_m \cos(\theta_m)$$

$$k_m^{\text{eff}} = \sqrt{(k_z^m)^2 - 2i\alpha k_z^m + \beta^2 - \alpha^2}$$

where k_m is the wave number of light in the medium surrounding the particles, ρ is the number density of particles in the suspension, and θ_m is the direction of light in this medium. Note that when the initial medium is introduced into the model, such that there is a boundary between this and the turbid medium containing the particles, θ_m is then the angle of refraction.

Experimentally we have control of the volume filling fraction, f, of the particles and this is related to the number density of particles, ρ, and the particle radius, a_0 via:

$$\rho = \frac{3f}{4\pi a_0^3}$$

[6]The exclusion volume of a particle is the volume that is inaccessible to other particles in the system as a result of the presence of the first particle.

Now let us consider what happens when we introduce the initial medium, placing the boundary at $z = 0$ and the turbid suspension at $z > 0$. The compound reflectance at the boundary [4] is then given by:

$$r = \frac{r_{12}^{\text{fresnel}} + r_{hs}(\theta_m) exp(2in_m k_0 \cos(\theta_m) a_0)}{1 + r_{12}^{\text{fresnel}} r_{hs}(\theta_m) exp(2in_m k_0 \cos(\theta_m) a_0)}$$

where θ_m is obtained from Snell's Law:

$$\theta_m = \arcsin\left(\frac{n_1}{n_m}\sin(\theta_i)\right)$$

k_0 is the vacuum wavenumber and r_{12}^{fresnel} is the Fresnel reflectivity that would arise at the boundary if the suspension contained no particles. Note that the phase factor $exp(2in_m k_0 \cos(\theta_m) a_0)$ arises as a result of the condition that no particles protrude into the region $z < 0$, and hence the centre of all particles must lie in the region $z > a_0$.

5 Monte Carlo Simulations: CSM

Error Source	Error Term Value	Standard Deviation in fiited $Re(n_p)$
Laser Power (1)	$\sigma_{LP} = 0.71\%$	0.0037
Angular Arm Position (2)	$\sigma = 0.1^\circ$	0.0138
Angular Arm Position (3)	$\sigma = 0.05^\circ$	0.0069
Combined 1,2		0.0143
Combined 1,3		0.0079

Table 4: Monte Carlo error propogation results, for 250 nm radius particles and $f = 3.6\,\%$.

This Monte Carlo analysis is similar to that outlined in Section 3.4.1, except that the forward model used is CSM and the fitting procedures used replicate those used for analysis of the real CSM data (below). Included here is a table of the results for 250 nm radius particles, with $f = 3.6\,\%$, but Monte Carlo analysis was performed replicating all experimental data obtained and is included in Appendix B. The table includes error propagation results for an angular arm uncertainty of $\sigma = 0.05^\circ$ as the value of $\sigma = 0.1^\circ$ may be an overestimate.

6 Method

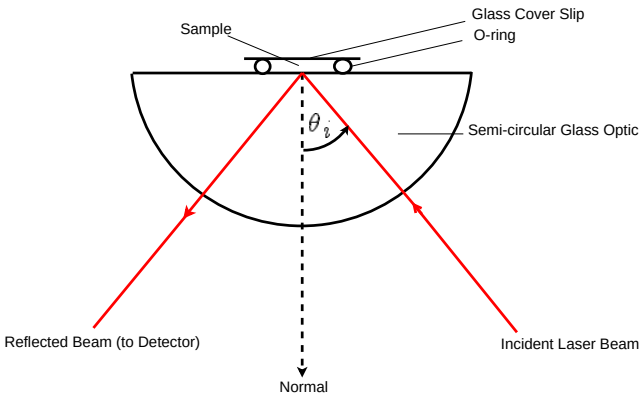

Figure 5: Diagram of experimental set-up.

The aim is to obtain reliable reflectance data for a range of incidence angles for the glass-suspension boundary. The experimental set-up is shown in Figure 5. The same scan procedure used for the glass-air measurements was applied here.

For the CSM theory presented above to be utilised for retrieving the refractive index of the particles from the reflectivity data, a dilute suspension of monodisperse particles in distilled water needed to be prepared.

The test particles used were polystyrene latex beads produced by Sigma-Aldrich, UK. The samples provided were in a concentrated form of 10 % w/w (±0.5 %) latex to water. The sample also contain between 0.3 to 1.5 % of a soluble polymer[7], used to stabilise the particles against flocculation and agglomeration. The samples are essentially monodisperse: the 250 nm radius particles have a coefficient of variation in size of $\leq$ 3 %, and the value is $\leq$ 5 % for the 500 nm radius particles.

It was found that the sample preparation procedure was crucial in determining the quality of the data obtained. The 10 % w/w suspensions were held in an ultrasonic bath for 15 seconds before any samples were made up, as recommended by the manufacturer. Diluted samples were made by adding several drops of the 10 % suspension to a vial, measuring the weight, then adding distilled water and re-measuring the weight (Scales accurate to 0.0001 g were used). These measurements allowed the volume filling fraction, f, to be calculated for the latex particles in the sample.

Firstly measurements were made using the 250 nm radius particles. Initially several samples were made up at the start of the day for various dilutions. These samples were then used throughout the day for scans. However it was found that this preparation gave results inconsistent with CSM theory (see Figure 6) and it was hypothesised that the samples were deteriorating with time. This may have been due to the fact that when the sample is diluted, its stability against flocculation and agglomeration reduces (the manufacturer also warns that this may be the case).

It was decided that samples should be prepared directly before the scan. The 10 % w/w suspension was held in the ultrasonic bath for 15 seconds as before, and then the dilution was made up. The diluted sample was then held in the ultrasonic bath for 5 mins. It was found that both preparing the sample directly before the scan and holding the diluted sample in the ultrasonic bath for 5 mins were necessary.

For the 500 nm particles the settling velocity of the particles becomes significant over the duration of the scan. Stokes' Law can be used to obtain the settling velocity of a spherical particle in a fluid [19]. The values obtained for 250 nm and 500 nm radius particles are 0.03 mm/hour and 0.17 mm/hour respectively. The height of the sample drop on the top of the optic is approximately 1 mm and the scan time is 1.5 hours. Thus for a scan time of 1.5 hours the settling velocity for the 500 nm particles is significant. This was only realised after there were difficulties fitting data.

In light of this it was decided that the scan procedure for 500 nm particles should be changed. An increased resolution scan over a small range of incidence angles about the critical angle was appropriate as it would reduce the scan time, and because the reflectivity curve is most sensitive to the particles' contribution close to the critical angle.

[7] This is likely to change slightly the refractive index of the water and is discussed further in Section 7.

Unfortunately, it was not possible to obtain as much data as would have been preferable for the 500 nm radius particles in the time available, and much of the data was obtained before realising the significance of the increased settling velocity for 500 nm particles.

7 Results

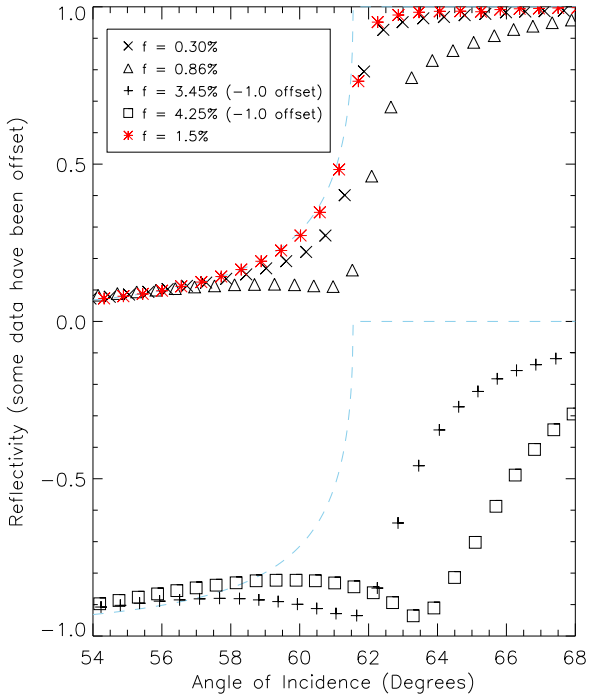

Figure 6: Reflectivity data obtained for samples that had deterioirated with time. There is a characteristic curve shape, that could not be reproduced by CSM theory. The red data shown were obtained with the improved sample preparation procedure. The blue dashed line shows the water reflectivity curve, and is included for reference.

Figure 6 shows examples of scan data obtained without the improved sample preparation procedure for various values of the volume filling fraction f. It was found that both preparing the sample directly before the scan, and holding the diluted sample in an ultrasonic bath, were necessary. Without both of these, data with the characteristic curve shape shown in Figure 6 were obtained. The curves have a large displacement to the right from the glass-water critical angle. Figure 6 includes a scan obtained with improved sample preparation in red for reference. This curve lies significantly closer to the critical angle.

Such curves could not be reproduced with CSM theory. One possible explanation is that the particles in the diluted sample undergo agglomeration with time. Attempts were made to test whether CSM theory could reproduce such curves for very large particle sizes $\geq 1\,\mu$m, but unfortunately the Mie scattering algorithm employed for calculating $S_j(\theta_s)$ was unable to cope with such large particles sizes.

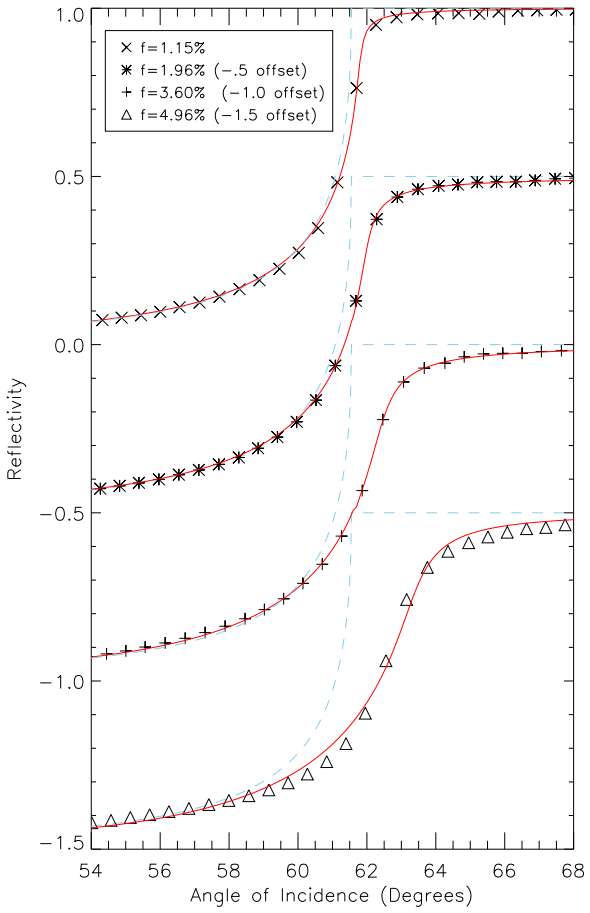

Figure 7: Reflectivity data for the latex suspension of 250 nm radius particles obtained with the improved sample preperation technique. The fitted CSM curves are shown in red and water reflectivity curves are shown in blue for reference. Note that some data have a reflectivity offset as specified in the key.

Figure 7 shows data obtained with the improved sample preparation procedure. The fit-

Fitted f (percentage)	Fitted $Re(n_p)$	Discrepancy $\Delta Re(n_p)$	Fitted $Re(n_{water})$	Fitted $Im(n_{water})$	σ Residual (percentage)
1.15	1.58660	0.00042	1.33215	0.00000	0.42
1.96	1.58521	0.00181	1.33257	0.00053	0.43
3.60	1.59390	-0.00688	1.33340	0.00044	0.31
4.96	1.62652	-0.03950	1.34103	0.00006	0.82

Table 5: Fitting results for the 250 nm radius particles.

ted CSM curves are shown in red. Note that experimental data were taken over a much larger range of incidence angles than those displayed in Figure 7, and the fitting procedure was implemented on the full set of data. The reflectivity curves deviate most significantly from the glass-water curve at incidence angles close to the glass-water critical angle. Table 5 displays the results of the fitted CSM curves. A least squares fitting procedure was used. The real part of the particle refractive index, $Re(n_p)$, was allowed to vary, but the imaginary part, $Im(n_p)$, was fixed at its known value of 0.000 [15]. The imaginary part was fixed because when allowed to vary the fitting procedure was prone to deviating to unphysical values.

It was found that allowing the refractive index of water ($n_{\text{water}} = n_m$ in the CSM forward model) to vary greatly improved the fit. This is physically sensible given that there is 0.3 to 1.5 % of polymer dissolved in the original 10 % w/w sample. The fitted values for the refractive index of water are included in Table 5. The volume filling fraction f was also allowed to vary over a small range, namely ± 5 %, corresponding to the uncertainty in the concentration of the original un-diluted sample.

It can be seen from Figure 7 that CSM provides a good fit to the data for $f = 1.15$ %, $f = 1.96$ % and $f = 3.60$ %. The fit is visibly less good for $f = 4.96$ %, and the experimental data deviate noticeably from the best-fit curve. Furthermore, this is illustrated by an approximate doubling of the σ Residual for the $f = 4.96$ % data compared to the data obtained for lower f. This suggests that the dilute approximation of CSM is no longer valid at a volume mixing ratio of $f = 4.96$ % for the 250 nm radius particles.

The fitted $Re(n_p)$ values for $f = 1.15$ %, $f = 1.96$ % and $f = 3.60$ % displayed in Table 5 compare well with the known value of $n(\lambda$=635nm) = 1.58702 [16]. The discrepancies for these volume filling fractions are within one standard deviation according to the error analysis.

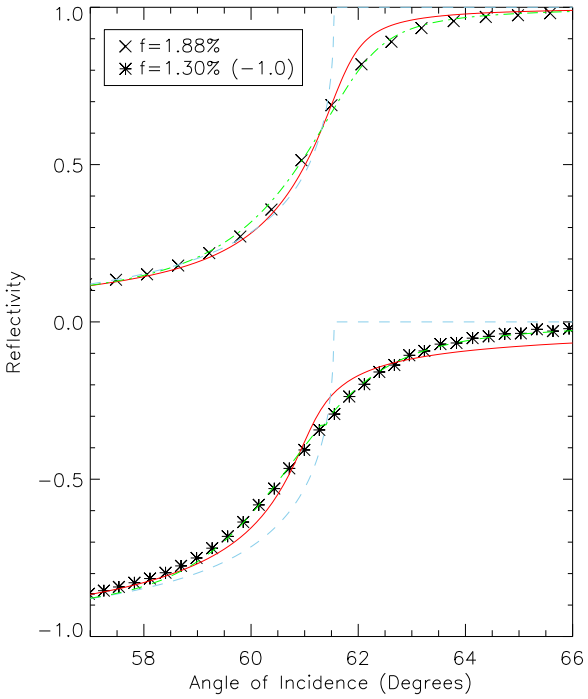

Figure 8: Reflectivity data for 2 scans with the 500 nm radius particles. The red curve is the CSM best-fit curve produced when $Re(n_p)$ was allowed to vary. The green curve is the best fit curve produced when $Re(n_p)$ is fixed but f is allowed to vary.

Figure 8 shows data obtained for the 500 nm radius particles for measured volume filling fractions $f = 1.30$ % and $f = 1.88$ %. Both scans

f measured (percentage)	Fitting Method (1) Fitted $Re(n_p)$	σ residual (1) (percentage)	Fitting Method (2) Fitted f	σ residaul (2) (percentage)
1.30	1.70	1.02	8.58	0.51
1.88	1.72	1.16	4.41	0.50

Table 6: Fitting Results for 2 scans of 500 nm radius particles affected by particle settling. Method 1: $Re(n_p)$ allowed to vary, and f fixed. Method 2: f allowed to vary, but $Re(n_p)$ fixed at known value. The $f = 1.30\,\%$ scan was at higher resolution and lasted twice as long.

were only over a small range of incidence angles about the glass-water critical angle, but the $f = 1.88\,\%$ scan was at a lower resolution compared to the $f = 1.30\,\%$ scan. Thus the duration of the $f = 1.30\,\%$ scan was twice that of the $f = 1.88\,\%$ scan.

The red curves were produced using the same fitting procedure (outlined above) used for the 250 nm radius particles. The data deviate noticeably from the red curve for both values of f. The fitted values for $Re(n_p)$ according to this procedure are shown in Table 6 (Fitting Method (1)), and deviate significantly from the known value. It is hypothesised that particle settling was affecting the data.

This hypothesis was tested by implemented a fitting procedure in which $Re(n_p)$ was fixed at its known value, but the volume filling fraction f was allowed to vary. The best fit curves for this fitting procedure are shown in green. The fitted values of f were significantly higher than the measured values as shown in Table 6. The fit is much improved with this method, as can be seen from the graph and correspondingly the σ Residual is approximately half that of the first fitting method. A possible explanation is that since the contribution to the reflectivity is greatest from particles closer to the glass-suspension interface, as the particles settle and accumulate towards this interface they give rise to a reflectivity curve expected for higher f in a properly dispersed suspension. The fact that the longer duration, higher resolution scan, which had a lower measured f, returned a higher fitted value by approximately a factor of two further supports the hypothesis that the results are affected by the continuous process of settling.

Figure 9 shows data for the final scan performed on the 500 nm radius particles. The time

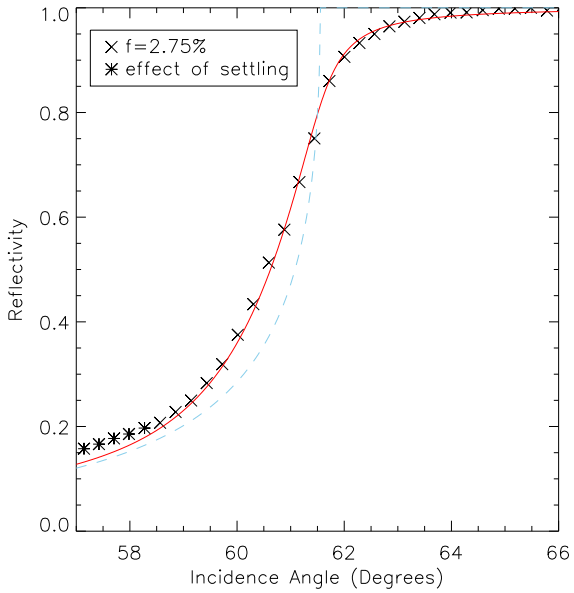

Figure 9: Scan for 500 nm radius particles with reduced time between preperation and start of scan. The red curve is fitted allowing $Re(n_p)$ to vary. The effect of settling becomes noticeable towards the end of the scan.

between preparation of the sample and the start of the scan was reduced by having the laser and detector arms pre-placed at their start positions rather than at their zero points. The data were fitted allowing $Re(n_p)$ to vary with the same procedure used for the 250 nm suspension. The fitted value returned was $Re(n_p) = 1.59273$, corresponding to a discrepancy of 0.00571 with the known value. This is within one standard deviation according to the error analysis (Appendix B). It can be seen from Figure 9 that there are 5 points that deviate noticeably from the fitted curve. This is likely the effect of particle settling. These points were not included in the fitting procedure. This highlights the importance of minimising the time between sample preparation and the start point of the scan, required to

obtain reliable data in this case where the settling velocity of the particles is significant.

In summary, it has been found that the sample preparation method is crucial in obtaining reliable data. With the improved sample preparation method, CSM fits well the experimental data for the 250 nm radius particles for a volume filling fraction up to $f = 3.60\,\%$, and was able to accurately retrieve the real part of the refractive index of these particles (to within uncertainties predicted by the Monte Carlo analysis). The settling velocity of the 500 nm radius particles posed a significant problem in obtaining reliable data for these suspensions. The results indicate that further measures are needed to improve the experimental method for such particles.

8 Conclusions

The results for the 500 nm particles indicate that there are difficulties that need to be overcome in future work on particles where the settling velocity is significant. Although some improvements were made, by reducing the time between sample preparation and the start of the scan, further improvement in the experimental method for large particles is needed.

One possibility, suggested by my supervisor, would be to place an ultrasonic oscillator in contact with the optic. This would mean particles in a suspension placed on top of the optic would be kept evenly distributed.

The end goal is using the apparatus and applying the coherent scattering model to retrieve the refractive index of aerosols at $\lambda = 635\,\text{nm}$. This will require an experimental procedure that negates the settling velocity issue. In addition, a typical aerosol sample, for example that of Saharan dust, does not have a monodisperse size distribution. Typically such samples have a log-normal size distribution. The precise distribution can be established from measurements using an Optical Particle Counter or a Differential Mobility Particle Sizer [20, 21]. It is possible to extend the coherent scattering model to polydisperse suspensions [4], by altering the expression for α and β (see Section 4) to:

$$\alpha = \frac{-2\pi}{k_m^2 \cos(\theta_m)} \int_0^\infty \rho(a) S_a(0)\,\mathrm{d}a$$

$$\beta = \frac{-2\pi}{k_m^2 \cos(\theta_m)} \int_0^\infty \rho(a) S_{j,a}(\pi - 2\theta_m)\,\mathrm{d}a$$

I have obtained experimental data for the reflectance of light from monodisperse suspensions of latex particles, of a known refractive index, in distilled water. The experimental data was obtained in an internal reflection configuration over a range of incidence angles, using a semi-circular glass optic and with the suspension placed on the top, flat surface. Experimental data was obtained individually for 250 nm and 500 nm radius monodisperse suspensions.

Although by no means exhaustive, the results obtained for the 250 nm particles support the validity of the coherent scattering model (CSM) up to a volume filling fraction of $f = 3.60\,\%$. The refractive index of these particles was retieved to within experimental uncertainty (as propagated using Monte Carlo analysis). To my knowledge CSM has not yet been tested on particles as large as this.

9 Acknowledgements

Thanks to Dr. D. Peters and Dr. R. Grainger, of the AOPP department, University of Oxford, for their help with this project.

References

[1] IPCC Fourth Assessment Report: Climate Change 2007. Working Group 1 Report, "The Physical Science Basis". Technical Summary, Aerosols.

[2] Aerosol spectroscopy Fire, Earth, Air and Water. D.M., Peters, R.A., McPheat, R.G., Grainger, G., Thomas, R., Irshad. University of Oxford, AOPP Department.

[3] Atmospheric Radiation: Molecules, Aerosols, and Clouds. Don Grainger. Lecture Handout. University of Oxford.

[4] "Coherent reflection of light from a turbid suspension of particles in an internal reflection configuration: Theory versus experiment". Augusto Garcia-Valenzuela, Ruben G. Barrera, Celia Sanchez-Perez, Alejandro Reyes-Coronado, and Eugenio R. Mendez. 5 September 2005/Vol. 13, No. 18/OPTICS EXPRESS 6724.

[5] "Coherent reflectance in a system of random Mie scatters and its relation to the effective-medium approach". Ruben G. Barrera, Augusto Garcia-Valenzuela. J. Opt. Soc. Am. A/Vol. 20, No. 2/February 2003.

[6] Topics in remote sounding. Theory of reflectance and emittance spectroscopy. Bruce Hapke. pg45.

[7] "The refractive index of colloidal sols". A. Chou and M. Kerker. J. Phys. Chem. 60, 562 (1956).

[8] "Determination of refractive indices of porcine skin tissues and intralipid at eight wavelengths between 325 and 1557 nm". H. Ding, J.Q. Lu, K. M. Jacobs, X-H Hu. J. Opt. Soc. Am. A 22 (6), 1151 (2005).

[9] "Refractive index measurement of absorbing and turbid fluids by reflection near the critical angle". G. H. Meeten and A. N. North. Meas. Sc. Technol. 6, 214(1995).

[10] "Applicability of effective medium theories to problems of scattering and absorption by non-homogeneous atmospheric particles". C.F. Bohnen. J. Atmos. Sci. 43, 468 (1986).

[11] "Optical reflectance of a composite medium with a sparse concentration of large spherical inclusions". A. Garcia-Valenzuela and R. G. Barrera. Phys. Status Solidi B 240, 480 (2003).

[12] "Effective propagation constants for coherent electromagnetic waves propagating in media embedded with dielectric scatters". L. Tsang and J. A. Kong. J. Appl. Phy. 53, 7162 (1982).

[13] Scattering of Electromagnetic Waves: Advanced Topics (Wiley, New York, 2001). L. Tsang and J. A. Kong.

[14] Light Scattering by Small Particles. Chap. 9: Rigorous Scattering Theory for spheres of arbitary size (Mie Theory). H. C. vand de Hulst.

[15] "Determination of complex refractive index of polystyrene microspheres from 370 to 1610 nm". Xiaoyan Ma et al 2003 Phys. Med. Biol. 48 4165.

[16] "Analysis of the dispersion of optical plastic materials". S. N. Kasarova et al. Optical Materials 29, 1481-1490 (2007).

[17] Refractive Index Database (http://refractiveindex.info/). Sumitra Optical Glass Data Book. Sumitra Optical Glass, Inc.

[18] "Optical Constants of Water in the 200 nm to 200 μm Wavelength Region". G. M. Hale and M. R. Querry. Appl. Opt. 12, 555-563 (1973).

[19] Light Scattering by Particles in Water: Theoretical and Experimental Foundations. M. Jonasz and G. Fournier. Elseiver Acedemic Press (2007).

[20] "A new instrument for stratospheric aerosol measurement". Thomas, GE. PhD Thesis. University of Canterbury. 2003.

[21] "Aerosol measurement: principles, techniques, and applications". Willeke, K., Baron P. A. Van Nostrand Reinhold, 1993.

A Appendix: Apparatus

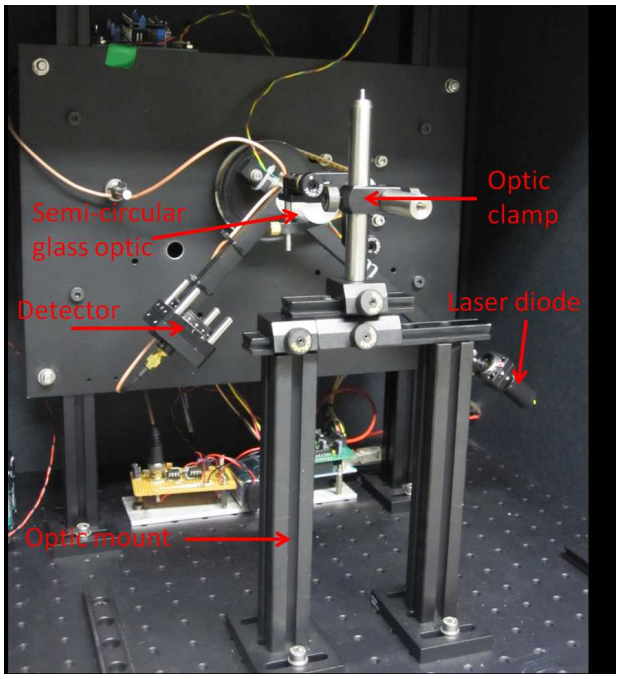

Figure 10: Photograph 1 of apparatus.

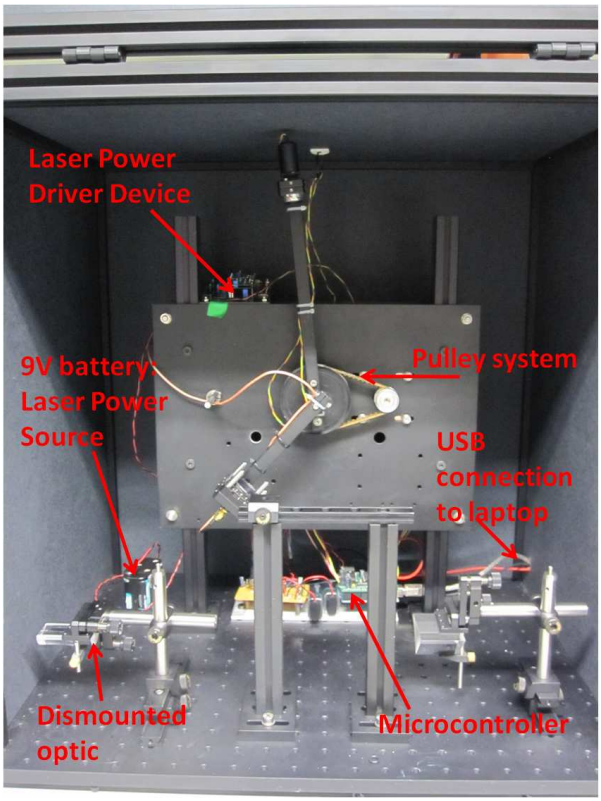

Figure 11: Photograph 2 of apparatus.

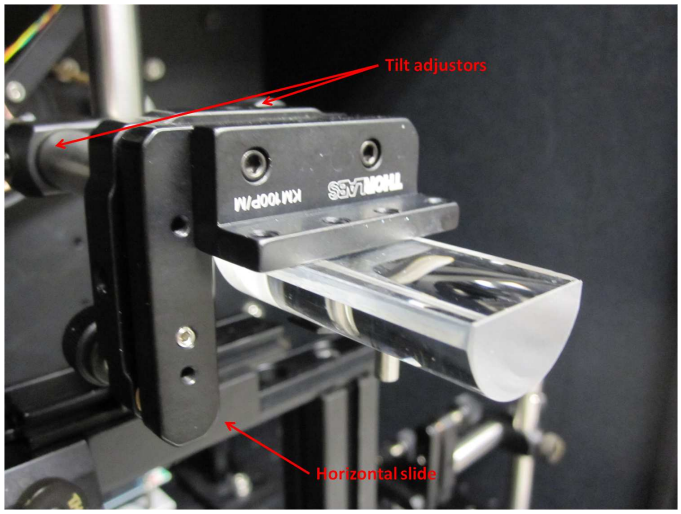

Figure 12: The semi-circular glass optic.

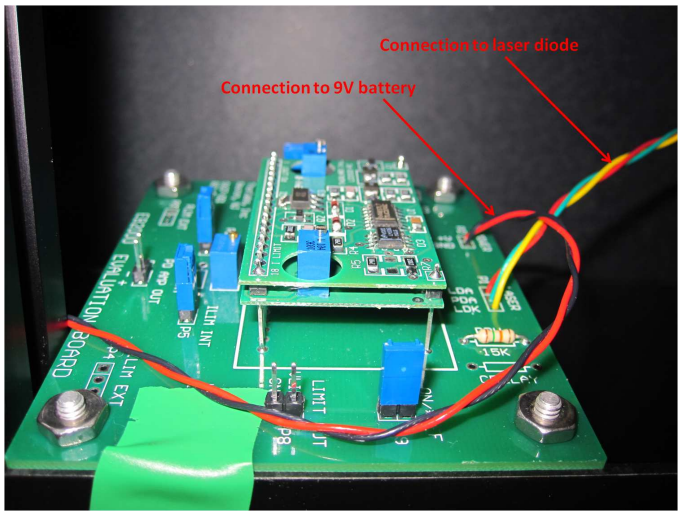

Figure 13: Thorlabs EK2000 laser power driver kit.

B Appendix: Monte Carlo Simulation Results, CSM

Error Source	Error Term Value	Standard Deviation in fiited $Re(n_p)$
Laser Power (1)	$\sigma_{LP} = 0.71\%$	0.0053
Angular Arm Position (2)	$\sigma = 0.1^\circ$	0.0269
Angular Arm Position (3)	$\sigma = 0.05^\circ$	0.0124
Combined 1,2		0.0274
Combined 1,3		0.0135

Table 7: Monte Carlo Error Propogation Results, for 250 nm radius particles and $f = 1.15\,\%$.

Error Source	Error Term Value	Standard Deviation in fiited $Re(n_p)$
Laser Power (1)	$\sigma_{LP} = 0.71\%$	0.0045
Angular Arm Position (2)	$\sigma = 0.1^\circ$	0.0198
Angular Arm Position (3)	$\sigma = 0.05^\circ$	0.0089
Combined 1,2		0.0203
Combined 1,3		0.0099

Table 8: Monte Carlo Error Propogation Results, for 250 nm radius particles and $f = 1.96\,\%$.

Error Source	Error Term Value	Standard Deviation in fiited $Re(n_p)$
Laser Power (1)	$\sigma_{LP} = 0.71\%$	0.0037
Angular Arm Position (2)	$\sigma = 0.1^\circ$	0.0138
Angular Arm Position (3)	$\sigma = 0.05^\circ$	0.0069
Combined 1,2		0.0143
Combined 1,3		0.0079

Table 9: Monte Carlo Error Propogation Results, for 250 nm radius particles and $f = 3.60\,\%$.

Error Source	Error Term Value	Standard Deviation in fiited $Re(n_p)$
Laser Power (1)	$\sigma_{LP} = 0.71\%$	0.0034
Angular Arm Position (2)	$\sigma = 0.1^\circ$	0.0104
Angular Arm Position (3)	$\sigma = 0.05^\circ$	0.0053
Combined 1,2		0.0109
Combined 1,3		0.0063

Table 10: Monte Carlo Error Propogation Results, for 250 nm radius particles and $f = 4.96\,\%$.

Error Source	Error Term Value	Standard Deviation in fiited $Re(n_p)$
Laser Power (1)	$\sigma_{LP} = 0.71\%$	0.0067
Angular Arm Position (2)	$\sigma = 0.1^\circ$	0.0256
Angular Arm Position (3)	$\sigma = 0.05^\circ$	0.0159
Combined 1,2		0.0265
Combined 1,3		0.0172

Table 11: Monte Carlo Error Propogation Results, for 500 nm radius particles and $f = 2.75\,\%$.